Quantitative Measurement of Two-phase Flow by Electrical Capacitance Tomography Based on 3D Coupling Field Simulation

Quantitative Measurement of Oil-gas Two-phase Flow by Electrical Capacitance Tomography Based on 3D Coupling Field Simulation

Shengnan Wang, Jiamin Ye, *Senior Member, IEEE*, and Yunjie Yang, *Member, IEEE*

***Abstract*—Measurement of oil-gas two-phase flow parameters such as Gas Void Fraction (GVF) and phase distribution plays a vital role in oil and gas industries. To quantitatively evaluate the performance of Electrical Capacitance Tomography (ECT) for measuring the complex dynamic oil-gas two-phase flows, a three-dimensional fluid dynamics-electrostatic field coupling model (3D-FECM) is proposed in this paper. Coupling simulation are carried out with a 12-electrode ECT sensor. Utilizing the 3D-FECM, the dynamic oil-gas two-phase flows and instantaneous ECT measurements are simultaneously obtained. Two GVF measurement approaches, i.e. the capacitance-based method and the image-based method, are used to calculate GVF. The permittivity distribution is reconstructed by using Linear Back Projection (LBP) and Landweber iteration. The capacitances with signal-noise ratios (SNRs) of 40 and 60 dB are generated for comparison and verification. Evaluation results show that the structural similarity between the ground truth and the reconstructed images using noise-free data by Landweber iteration are better than 0.765, while those by LBP are higher than 0.754, the noise with SNR of 60 dB has no obvious effect on the performance of image reconstruction, and the full-scale error of the image-based GVF prediction using 60 dB noisy data is within -0.82% to +6.09%, slightly better than that of the capacitance-based GVF results (i.e. -1.16% to +7.63%).**

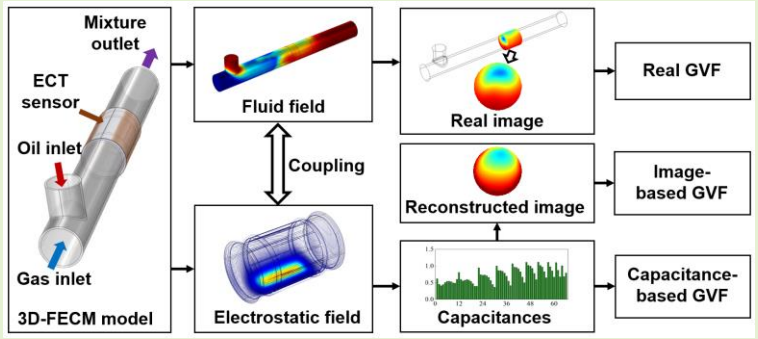

***Index Terms*—Oil-gas two-phase flow, electrical capacitance tomography, three-dimensional, fluid dynamics-electrostatic field coupling, gas void fraction, reconstructed image.**

I. Introduction

ELECTRICAL Capacitance Tomography (ECT) has attracted extensive interest in measuring oil-gas two-phase flows due to its ability to online visualize the complex flows and its advantages of simple structure, non-invasiveness, non-radiation, low cost and high applicability [1]-[4]. The principle of ECT is to reconstruct the permittivity distribution (usually dielectric materials) in the region of interest from the measured inter-electrode capacitances via certain inversion algorithms. Based on the reconstructed distributions, some key hydrodynamic parameters of the oil-gas two-phase flow such as Gas Void Fraction (GVF) and flow regimes can also be determined [5]-[7].

In the past decades, extensive efforts have been made in advancing ECT for measuring oil-gas two-phase flows [2], [8]-[10]. For instance, Ismail *et al.* built an ECT-based test rig to measure the interfaces in oil separators [8]. Gamio *et al.* developed a set of ECT apparatus with a high-pressure (1400 psi) sensor to monitor the oil-gas two-phase flow in industrial pressurized pipelines [9]. Li *et al.* reported the application of ECT in gas-oil two-phase flow measurement, and presented promising results on TUV-NEL's multiphase flow facility [10].

Despite these encouraging results, there still exists unresolved challenges to prevent ECT from achieving its full potential in flow measurement. The 'soft-field' effect, which describes the phenomenon that the electric field within the sensing region could be distorted by the dynamic flow, leads to the nonlinear ECT image reconstruction problem and

Manuscript received February 22, 2021; accepted XX XX, 2021. Data of publication XX XX, 2021; data of current version XX XX, 2021. This work was supported in part by the European Union's Horizon 2020 Research and Innovation Programme under the Marie Sklodowska-Curie actions COFUND Transnational Research And Innovation Network at Edinburgh under Grant 801215, and in part by the National Natural Science Foundation of China under Grant 51906209. (Corresponding author: Yunjie Yang)

S. Wang was with the College of Electrical, Energy and Power Engineering, Yangzhou University, Yangzhou 225127, China. He is now with the Agile Tomography Group, School of Engineering, Institute for Digital Communications, The University of Edinburgh, Edinburgh EH9 3FG, U.K. (e-mail: shengnan.wang@ed.ac.uk)

Y. Yang is with the Agile Tomography Group, School of Engineering, Institute for Digital Communications, The University of Edinburgh, Edinburgh EH9 3FG, U.K. (e-mail: Y.Yang@ed.ac.uk).

J. Ye is with the School of Electrical and Information Engineering, Tianjin University, Tianjin 300072, China. (e-mail: yejiamin_19@tju.edu.cn).

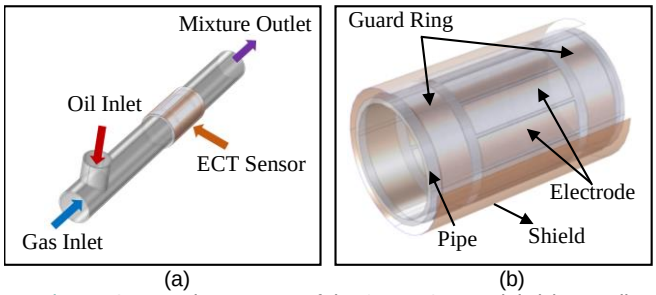

Fig. 1. Geometric structure of the 3D-FECM model. (a) overall structure. (b) ECT sensor.

unsatisfactory images [11]-[13]. The oil-gas two-phase flows in the petroleum industry are extremely unstable. As a result, the relationships between the dynamic flow parameters and the measured capacitances are too complicated to be analytically described by physical models. In practice, static simulation and experimental approaches are commonly adopted to investigate the relationships between the measured capacitances and the permittivity distribution [14]-[16], whilst more studies are required to approach the practical conditions. Another limiting factor in dealing with dynamic flows is the lack of access to the ground truth of permittivity distributions for quantitative performance evaluation [17]. Although many multiphase flow loops have been established for the assessment and calibration of flow sensors under a wide range of flow conditions, the real permittivity distributions and key flow parameters at the sensing section cannot be obtained instantaneously. To address this issue, Ye *et al.* proposed a simulation model by coupling the fluid field and electrostatic field for evaluating the performance of ECT on two-phase flows [17], [18]. However, the model in these works is limited to 2D liquid-solids flows with a 2D ECT sensor and the focus is to assess the image quality, which is still far from the real scenarios.

In this paper, a three-dimensional fluid dynamics-electrostatic field coupling model (3D-FECM) is developed to simulate dynamic oil-gas two-phase flows and a 3D ECT sensor with 12 electrodes is integrated to obtain corresponding ECT measurements in an instantaneous manner. The ECT measurements are first employed to estimate the GVF based on the prevailing model and reconstruct the volume-averaged permittivity distribution of the flow using commonly used algorithms. We then quantitatively evaluate the GVF estimation and the reconstructed image quality of ECT by employing a number of metrics. We aim to demonstrate the proposed method offers a promising platform to quantitatively evaluate the performance of ECT for measuring complex dynamic flows.

II. Three-dimensional Fluid Dynamics-electrostatic Field Coupling Model (3D-FECM)

A. Geometry Structure of the 3D-FECM

Fig. 1(a) shows the geometric structure of the 3D-FECM model. It consists of a vertical pipe with an internal diameter of 1.6 m, a horizontal pipe with an internal diameter of 2 m, and an ECT sensor mounted on the outer surface of the horizontal section. The schematic of the ECT sensor is shown in Fig. 1(b). It mainly consists of twelve arc-shaped electrodes (electrode coverage: 90%, electrode axial length: 2 m), two grounded guard rings and a grounded shield. The model has a gas inlet, an oil inlet and a mixture outlet. During the simulation, gas and oil are fed into the model through the two inlets, forming two-phase flows in the horizontal section, and then flow out from the mixture outlet.

B. Principle of Coupling Simulation

We adopt similar approaches with [17], [18] to couple the fluid and electrostatic fields. During the fluid dynamics-electrostatic field coupling simulation, the oil-gas two-phase flow data, generated by the fluid field interface model, is coupled to the electrostatic field model for the calculation of the electric potential distribution.

In the fluid field interface, the laminar flow model is applied to simulate the oil-gas two-phase flow, in which case the incompressible Navier-Stokes equations with surface tension and gravity take the form [19]:

$$\rho\frac{\partial \mathbf{u}}{\partial t}+\rho(\mathbf{u}\cdot\nabla)\mathbf{u}=\nabla\cdot\left[-p\mathbf{I}+\mu\left(\nabla\mathbf{u}+\nabla\mathbf{u}^{T}\right)\right]+\mathbf{F}_{g}+\mathbf{F} \quad (1)$$

$$\nabla\cdot\mathbf{u}=0 \quad (2)$$

where $\mathbf{u}$ is the mass averaged mixture velocity vector; $\mathbf{F}_g$ is the gravity force vector; $\mathbf{F}$ is the volume force vector; $\mathbf{I}$ represents the identity tensor; p is the pressure; ρ is the mixture density defined by

$$\rho=\rho_h+(\rho_l-\rho_h)\phi \quad (3)$$

and the mixture dynamic viscosity μ is given by

$$\mu=\mu_h+(\mu_l-\mu_h)\phi \quad (4)$$

where ρ_h and ρ_l are the densities of oil and gas, respectively; μ_h and μ_l are the dynamic viscosities of oil and gas, respectively, and ϕ is the gas void fraction.

We adopt the level set method [20] to track the moving interface between the oil phase and gas phase:

$$\frac{\partial\phi}{\partial t}+\mathbf{u}\cdot\nabla\phi=\gamma\nabla\cdot\left(\delta\nabla\phi-\phi(1-\phi)\frac{\nabla\phi}{|\nabla\phi|}\right) \quad (5)$$

where γ is the reinitialization parameter, and δ is the interface thickness controlling parameter (set to $h_{max}/2$, where h_{max} is the maximun element size in the component).

In electrostatic interface, the electric potential φ is determined by Poisson equation [21]:

$$-\nabla\left(\varepsilon_o\varepsilon_m\nabla\varphi\right)=0 \quad (6)$$

where ε_o represents the vacuum permittivity, and ε_m represents the equivalent permittivity of the mixing fluid. The Wiener Upper Bound formula is applied to evaluate the equivalent permittivity of the oil-gas mixture [22], which can be expressed as

$$\varepsilon_m=\varepsilon_l\phi+\varepsilon_h(1-\phi) \quad (7)$$

where ε_h and ε_l are the relative permittivity of oil and gas, respectively.

III. Measurement Principles

A. Principle of ECT

It can be deduced from (7) that the equivalent permittivity of the oil-gas mixture varies with different constituent contents.

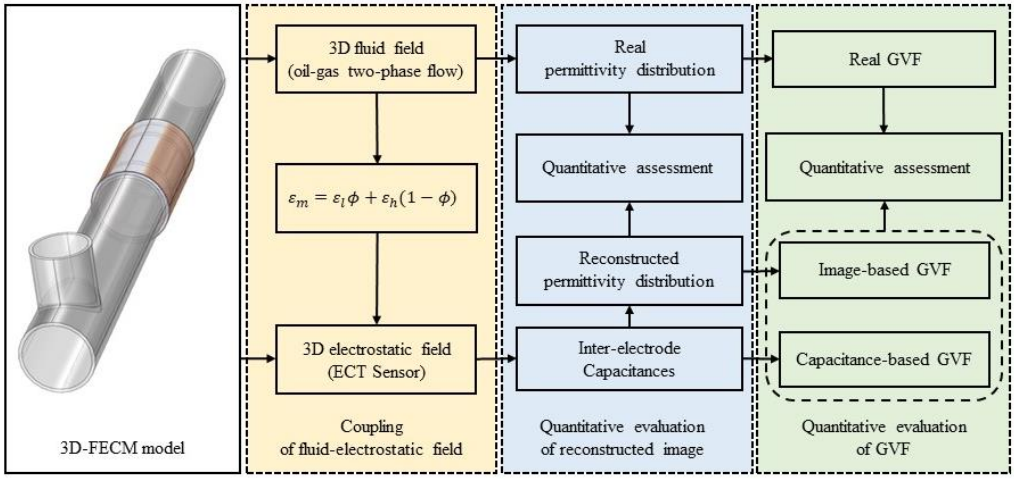

Fig. 2. Flowchart of coupling fluid dynamics-electrostatic field simulation.

When the oil-gas mixture passes through the sensing region of the ECT sensor, the capacitance between the excitation and detection electrodes will change with the permittivity distribution of the flow, which can be expressed as [23]:

$$C = \frac{Q}{V} = -\frac{1}{V}\iint_A \varepsilon(x,y,z)\nabla\varphi(x,y,z)dA \tag{8}$$

where (x, y, z) denotes the voxel coordinate of the sensing region of the ECT sensor; C is the capacitance of a pair of electrodes; V is the potential difference between the two electrodes; $\varepsilon(x, y, z)$ is the permittivity distribution in the sensing region; $\varphi(x, y, z)$ is the electric potential distribution, and A is the surface area of the detection electrode.

For a 12-electrode ECT sensor, a total of 66 independent capacitance measurements can be obtained, based on which the permittivity distribution of the oil-gas flow within the sensing region can be reconstructed using certain inversion algorithms. Under discrete and linear approximations, the ECT model can be written as a normalized form:

$$\lambda_n = Sg \tag{9}$$

where S is the normalized sensitivity matrix; g is the normalized permittivity, and λ_n is the normalized capacitance defined by

$$\lambda_n = \frac{C_m - C_m{}^l}{C_m{}^h - C_m{}^l} \tag{10}$$

where C_m is the raw measured capacitance; $C_m{}^h$ and $C_m{}^l$, respectively, denotes the measured capacitance when the sensing region is filled with oil and gas.

Linear Back Projection (LBP) is commonly used in ECT due to its simplicity and fast speed [24]. By implementing LBP, the estimated permittivity $\hat{g}$ can be calculated by

$$\hat{g} = S^T\lambda_n \tag{11}$$

Landweber iteration is widely recognized to be capable of reconstructing the best images in most cases [6], which can be implemented as

$$\hat{g}_{k+1} = P\left[\hat{g}_k - \alpha S^T(S\hat{g}_k - \lambda_n)\right] \tag{12}$$

$$P[f(x)] = \begin{cases} 0 & \text{if } f(x) < 0 \\ f(x) & \text{if } 0 \le f(x) \le 1 \\ 1 & \text{if } f(x) > 1 \end{cases} \tag{13}$$

where k is the iteration number; $\hat{g}_k$ is the estimated permittivity at the k^{th} iteration, and α is the relaxation factor.

B. Gas Void Fraction (GVF)

Two commonly used GVF estimation methods, including capacitance-based method and image-based method, are quantitatively evaluated.

1) *Capacitance-based Method*

According to the structure features of the ECT sensor (see Fig. 1(b)), the capacitance between the electrode pair essentially contains (1) the effective capacitance of the pipe wall C_W and (2) the oil-gas mixture capacitance C_x. It can be formulated as

$$\begin{cases} 1/C_m = 1/C_W + 1/C_x(\varepsilon_m) \\ 1/C_m{}^h = 1/C_W + 1/C_x(\varepsilon_h) \\ 1/C_m{}^l = 1/C_W + 1/C_x(\varepsilon_l) \end{cases} \tag{14}$$

Combining (10) and (14), it yields:

$$\lambda_n = \frac{C_x(\varepsilon_m) - C_x(\varepsilon_l)}{C_x(\varepsilon_h) - C_x(\varepsilon_l)} \tag{15}$$

The oil-gas mixture capacitance C_x is linearly related to the permittivity of the mixing fluid ε_m, i.e.

$$C_x(\varepsilon_m) = k\varepsilon_m \tag{16}$$

Similarly, for the pure oil flow and gas flow, we have

$$C_x(\varepsilon_h) = k\varepsilon_h \tag{17}$$

$$C_x(\varepsilon_l) = k\varepsilon_l \tag{18}$$

Inserting (16)-(18) into (15) gives

$$\lambda_n = \frac{\varepsilon_m - \varepsilon_l}{\varepsilon_h - \varepsilon_l} \tag{19}$$

Easily, we can derive that

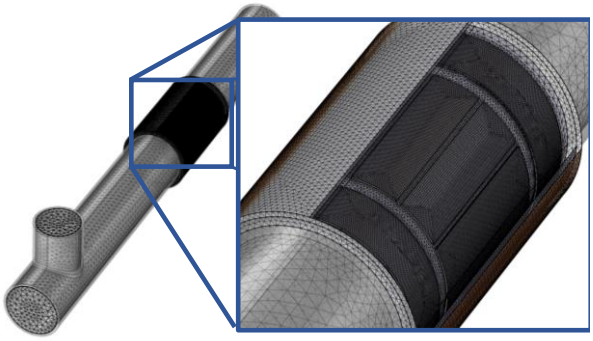

Fig. 3. Mesh of the 3D-FECM model.

TABLE I
FLUID FIELD SIMULATION SETUP

Parameters	Value	Description
V_h (m/s)	1, 2, 4	Inflow velocity of oil
V_l (m/s)	2	Inflow velocity of gas
T (K)	293.15	Temperature
ρ_h (kg/m^3)	879	Density of oil
ρ_l (kg/m^3)	1.3	Density of gas
μ_h (Pa·s)	0.02	Dynamic viscosity of oil
μ_l (Pa·s)	1.81E-5	Dynamic viscosity of gas

TABLE II
ELECTROSTATIC FIELD SIMULATION SETUP

Parameters	Value	Description
ε_h	2.8	Relative permittivity of oil
ε_l	1	Relative permittivity of gas
ε_{pipe}	2.6	Relative permittivity of pipe
A(V)	1	Amplitude of excitation voltage

$$\varepsilon_m = \lambda_n(\varepsilon_h - \varepsilon_l) + \varepsilon_l \tag{20}$$

This is then used in an alternative expression of (7) to calculate GVF.

2) *Image-based Method*

The cross-section sensing region is discretized into 3228 pixels. Image reconstruction is essentially to determine the normalized permittivity of each pixel from the 66 capacitance measurements. By averaging the reconstructed permittivity $\hat{g}$, the GVF can be obtained:

$$\phi = 1 - \frac{1}{3228}\sum_{i=1}^{3228}\hat{g}(i) \tag{21}$$

IV. FLUID DYNAMICS-ELECTROSTATIC FIELD COUPLING SIMULATION

A. Simulation Setup

Coupling fluid dynamics-electrostatic field simulation is performed using COMSOL Multiphysics and Matlab. Fig. 2 shows the flowchart of the coupling simulation. By coupling the fluid field and the electrostatic field, the dynamic permittivity distributions and the corresponding capacitances are obtained. The capacitances are used to calculate the GVF and reconstruct the volume averaged permittivity distributions. The estimated GVF and reconstructed images are finally quantitatively evaluated against the ground truth. To get grid-independent results, tetrahedral meshes consisting of 2,182,931 elements are generated (see Fig. 3).

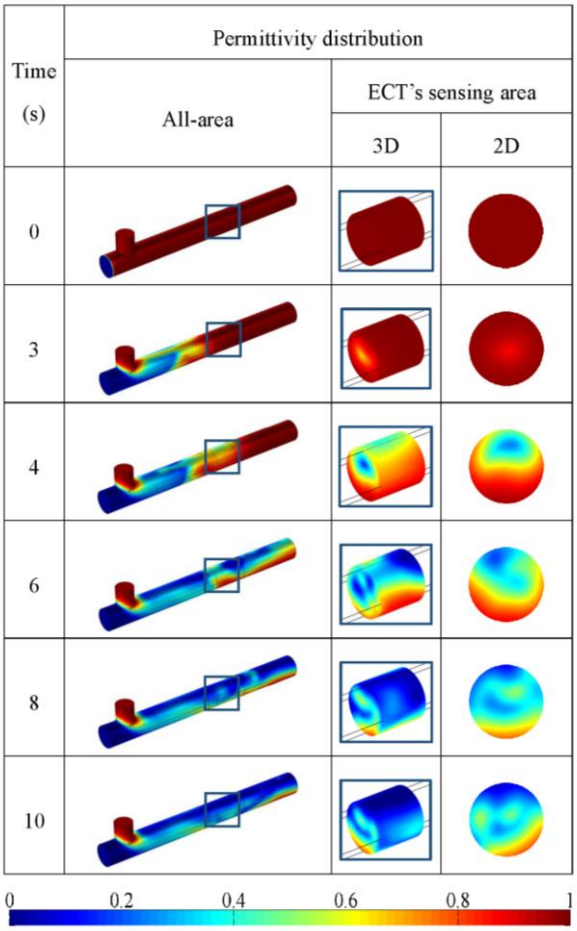

Fig. 4. Permittivity distributions obtained from coupling simulation (V_h = 2 m/s, V_l = 2 m/s).

For the fluid field simulation, the velocity inlet and pressure outlet boundary conditions are imposed to avoid convergence difficulties. The suppress backflow is selected to prevent fluid from entering the domain through the outlet boundary. No-slip condition is used as the wall boundary condition. The gas phase is air, the liquid phase is industrial white oil. To reduce the computational costs without deviating from flow's actual behavior, the temperature of the system is set to as a constant of 293.15 K, the oil-gas two-phase flow is set as incompressible flow, and the densities of each phase independent of the pressure. The density and the dynamic viscosity of the oil is 879 kg/m^3 and 0.02 Pa·s respectively. The density and the dynamic viscosity of the gas is 1.3 kg/m^3 and 1.81E-5 Pa·s respectively. The inlet gas and oil flow rates can be controlled by regulating the inlet velocities perpendicular to the faces. In this study, three different inlet oil velocities of 1, 2, 4 meters per second (m/s) with the inlet gas velocity of 2 m/s are chosen to simulate the gas-oil two-phase flows with different volumetric concentration. The simulation conditions for the fluid field simulation are summarized in TABLE I.

For the electrostatic field simulation, the relative permittivity of pipe, oil and gas is 2.6, 2.8 and 1, respectively. The excitation voltage with the value of 1V is alternately applied on

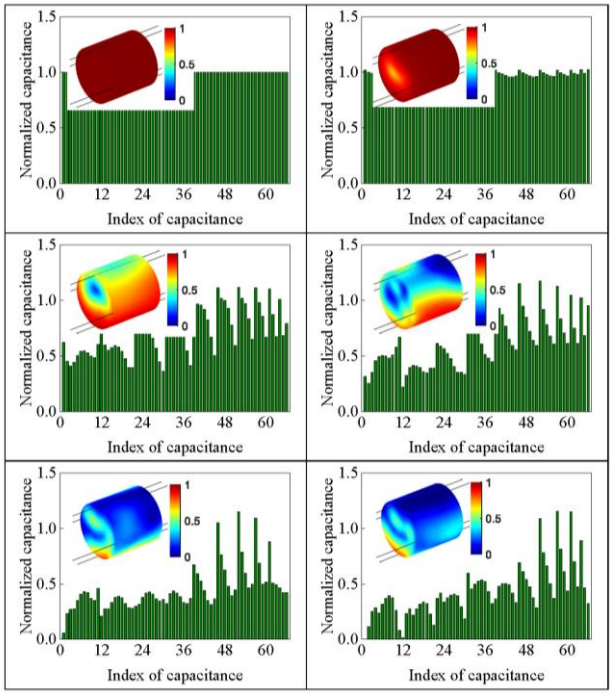

Fig. 5. Normalized inter-electrode capacitances obtained from coupling simulation.

TABLE III
OPERATION CONDITIONS FOR COMPARISON SIMULATION

	Case1	Case2	Case3	Case4	Case5	Case6
V_h (m/s)	1	2	4	1	2	4
Initial mode	Oil-mode			Gas-mode		

the electrodes for inter-electrode capacitance measurement. The details of the electrostatic field simulation setup are listed in TABLE II.

B. Simulation Results

Based on the 3D-FECM and the simulation setups described above, the time-varying permittivity distribution and corresponding capacitance measurements are collected. The 3D permittivity distribution in the sensing region of ECT can be extracted and converted to the 2D volume-averaged permittivity distribution by performing voxel-to-voxel average along the sensor's axial direction.

Fig. 4 shows the sequential permittivity distributions of the oil-gas flow with 1-2 s interval by the fluid-electric field coupling model when the inflow velocities of oil and gas are both configured as 2 m/s. It is found that the pipe is initially filled with oil. When the gas and oil feed into the model, two-phase flow is formed in the horizontal pipe section. With the further injection of the gas and oil, the laminar flow is gradually presented and flow out from the outlet. During the simulation, the permittivity distribution data obtained from fluid field model is coupled to the electric field model for the calculation of inter-electrode capacitance. Fig. 5 shows the calculated normalized inter-electrode capacitances corresponding to the permittivity distributions in Fig. 4. It is found that the normalized inter-electrode capacitances change significantly with the change of the permittivity distribution.

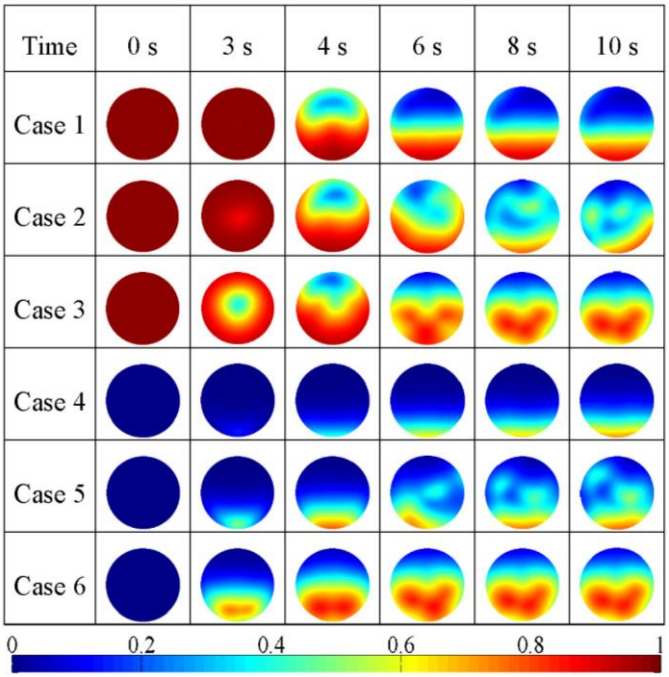

Fig. 6. Ture permittivity distributions obtained from coupling simulation with different V_h.

Extensive researches have expressed that the relationship between the capacitances and permittivity distribution is nonlinear and could be susceptible to the dynamic flow due to the soft-field effect of the ECT sensor [11], [13], [17].

By regulating the inlet oil velocity perpendicular to the entrance surface, the gas-oil two-phase flows with different volumetric concentrations can be simulated. Comparison experiments are also carried out with two initial modes: oil-mode and gas-mode. Oil-mode refers to the initial stage in which the pipe is filled with oil, and gas-mode refers to the initial stage in which the pipe is filled with gas. The corresponding operation conditions for these comparison simulations are summarized in TABLE III. Fig. 6 presents the sequential cross-sectional permittivity distributions of the oil-gas two-phase flow obtain from coupling simulation with different inlet oil velocities and different initial modes. From Fig. 6, it is obvious that, at the same time and under identical initial conditions, the oil holdup of the flow increases with the increasing of the inlet velocity of oil, and almost all flows present typical laminar character, indicating that the coupling model has high stability and validity for oil-gas two-phase flow simulation.

V. QUANTITATIVE EVALUATION AND DISCUSSION

A. Image Reconstruction

Two image reconstruction algorithms, i.e., the LBP and Landweber iteration, are used to reconstruct the cross-sectional permittivity distribution. The Landweber iteration algorithm has semi-convergence properties, which means that the image error decreases rapidly in the beginning of the iteration, while the image error increases as the iteration process continues. In this study, the real permittivity distributions have already known, so the optimal number of iterations can be determined.

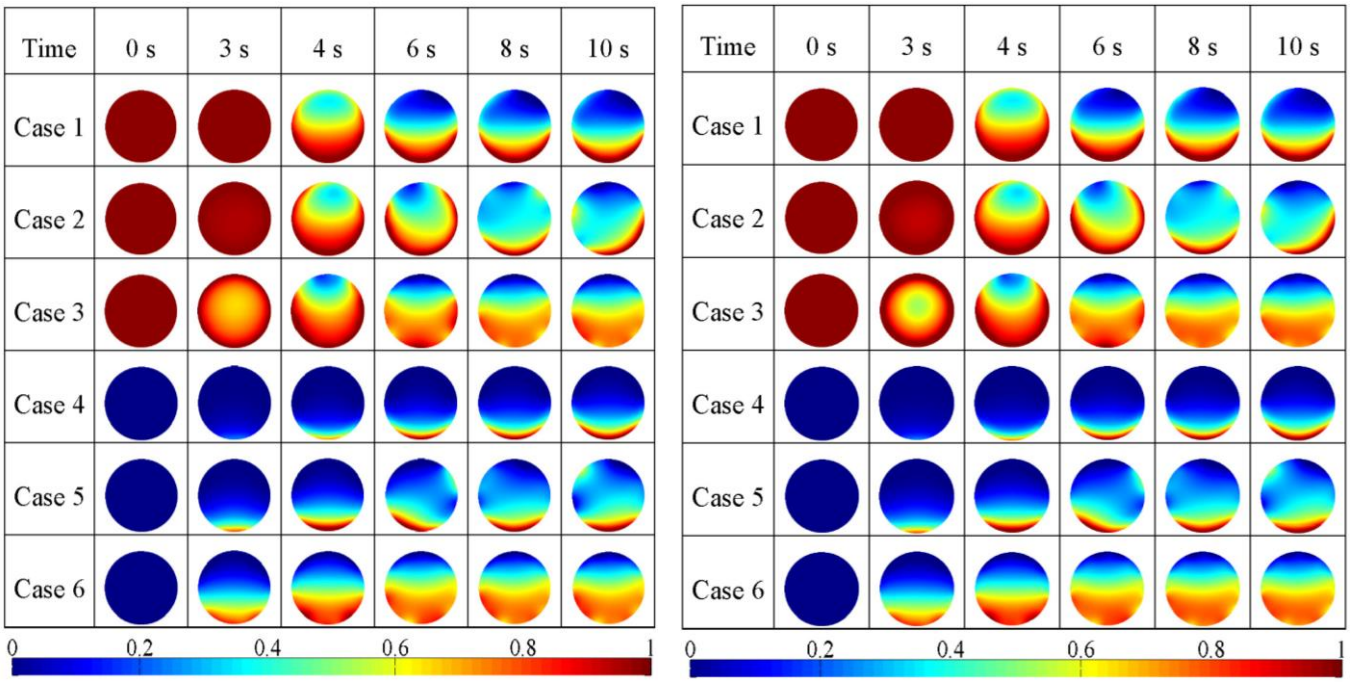

Fig. 7. Permittivity distributions reconstructed by different algorithms using noise-free capacitance data. (a) permittivity distributions reconstructed by LBP. (b) permittivity distributions reconstructed by Landweber iteration.

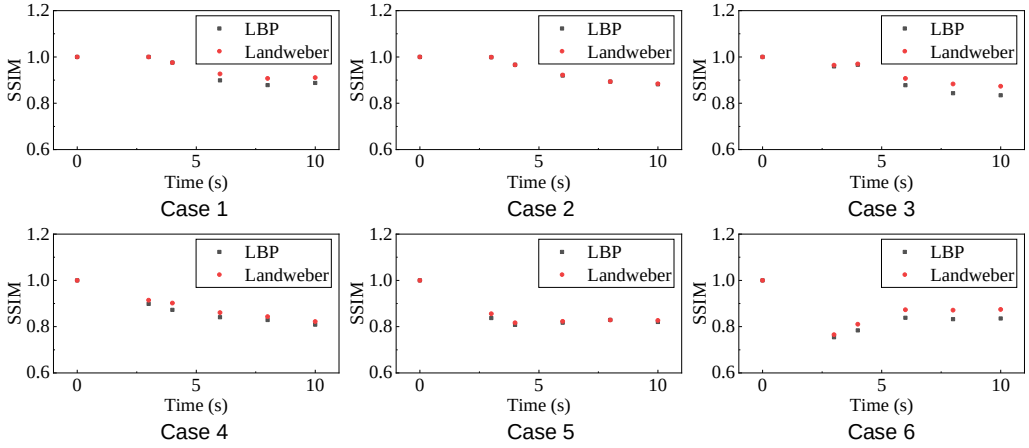

Fig. 8. Structural similarity of the sequential reconstructed images in Fig. 7.

TABLE IV
ITERATIONS NUMBER OF THE RECONSTRUCTED PERMITTIVITY DISTRIBUTIONS IN FIG. 7(B)

Time	0 s	3 s	4 s	6 s	8 s	10 s
Case 1	1	1	2	22	20	17
Case 2	1	313	2	7	2	12
Case 3	1	328	13	36	48	49
Case 4	1	30	17	13	10	8
Case 5	1	14	10	13	2	14
Case 6	1	20	25	44	49	47

In this paper, the images are reconstructed by using the optimal number of iterations for a relaxation factor of 1 during the Landweber iteration process.

The inter-electrode capacitances used for image reconstruction are obtained from the 3D-FECM coupling simulation. Figs. 7 (a) and (b) show the permittivity distributions reconstructed using LBP and Landweber iteration algorithms, respectively. The iterations numbers of the sequential reconstructed images in Fig. 7(b) are listed in TABLE IV. Compared with the true permittivity distributions in Fig. 6, it is found that both the reconstructed images from LBP and Landweber iterative are similar to the real images. To quantitatively evaluate the quality of the reconstructed images, the Structural Similarity Index Measure (SSIM) is introduced [25], which is defined as

$$\mathrm{SSIM}=\frac{(2\alpha_x\alpha_y+C_1)(2\sigma_{xy}+C_2)}{(\alpha_x^{\,2}+\alpha_y^{\,2}+C_1)(\sigma_x^{\,2}+\sigma_y^{\,2}+C_2)} \tag{22}$$

where α_x and α_y are the mean intensities of the real image and reconstructed image respectively; σ_x and σ_y are the variances of the real image and reconstructed image respectively; σ_{xy} is the

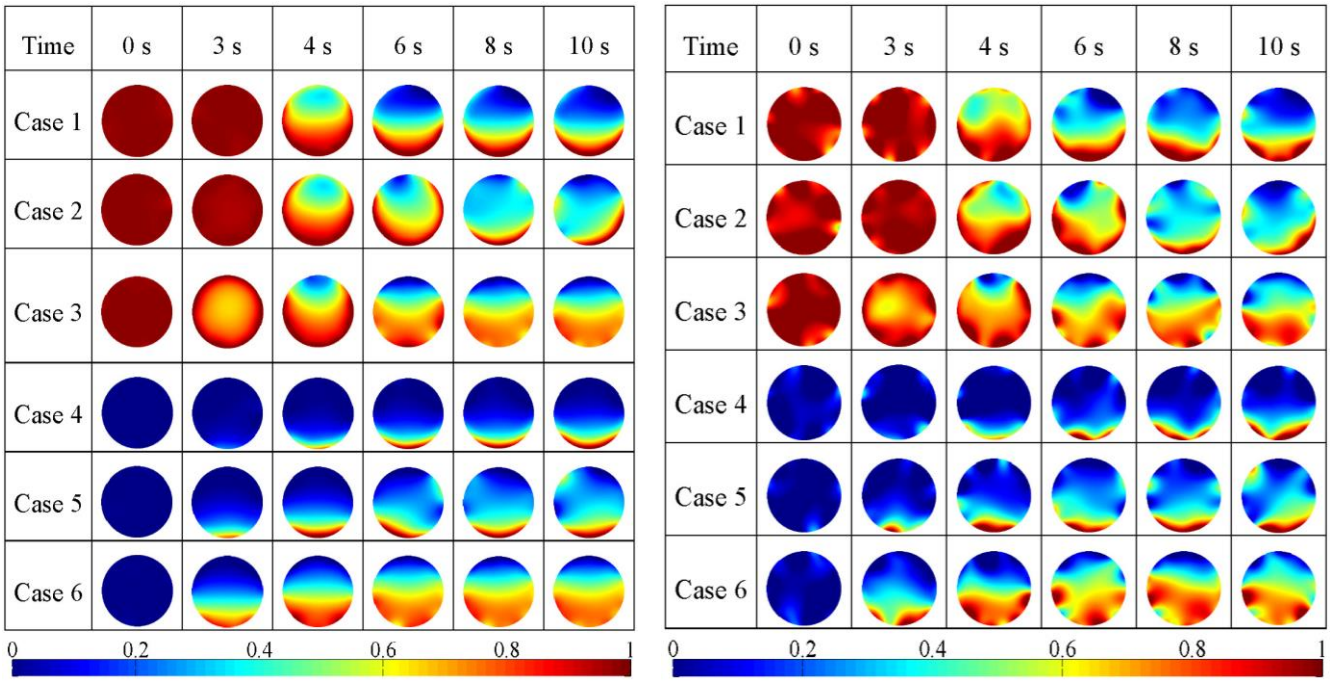

Fig. 9. Permittivity distributions reconstructed by LBP using noisy capacitance data. (a) 60 dB noisy data. (b) 40 dB noisy data.

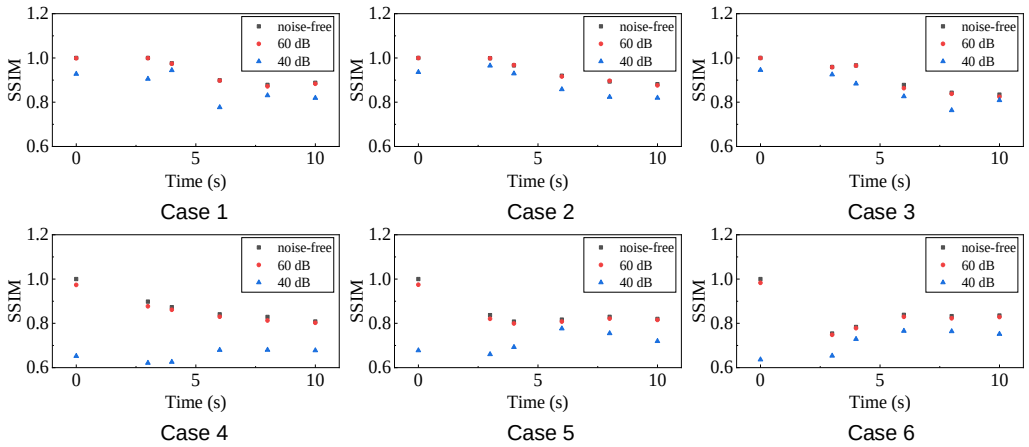

Fig. 10. Structural similarity of the sequential reconstructed images in Fig. 8.

covariance of the real image and reconstructed image; The constants C_1 and C_2 are included to stabilize the division when $\alpha_x^2+\alpha_y^2$ or $\sigma_x^2+\sigma_y^2$ is very close to zero.

SSIM offers an effective image quality assessment method by synthetically checking the images' luminance, contrast and structure. The closer the value of SSIM is to 1, the better the reconstructed results. Fig. 8 shows the SSIM of the sequential reconstructed images in Fig. 7. It can be seen that, in general, the images reconstructed by Landweber iterative have slightly better quality than those by LBP. The minimum value of the SSIM between the real images and reconstructed images from Landweber iteration is 0.765, and that from LBP is 0.754. Despite the similarities between the reconstructed images and the real images, differences also exist on them, especially in the case of low oil concentration. Although ECT technology is relatively mature and has been widely applied both in industry and laboratory, it still has the problem of relatively low-resolution imaging due to the ill-conditioned problem and the soft-field effect of ECT.

The capacitances obtained from the 3D-FECM coupling simulation is noise free. However, noise disturbance is inevitable in real capacitance measurement. Therefore, the capacitances with signal-noise ratios (SNRs) of 60 and 40 dB are generated for comparison and verification. Fig. 9 shows the images reconstructed by LBP using 60 and 40 dB noisy capacitance data, and the SSIMs of the sequential reconstructed images are presented in Fig. 10. It can be found that the reconstructed images using 60 dB noisy data are similar to those using noise-free data, and the values of the SSIM are very close to those from the noise-free data, indicating that the noise with SNR of 60 dB has no obvious effect on the performance of image reconstruction. For the 40 dB noisy data, the

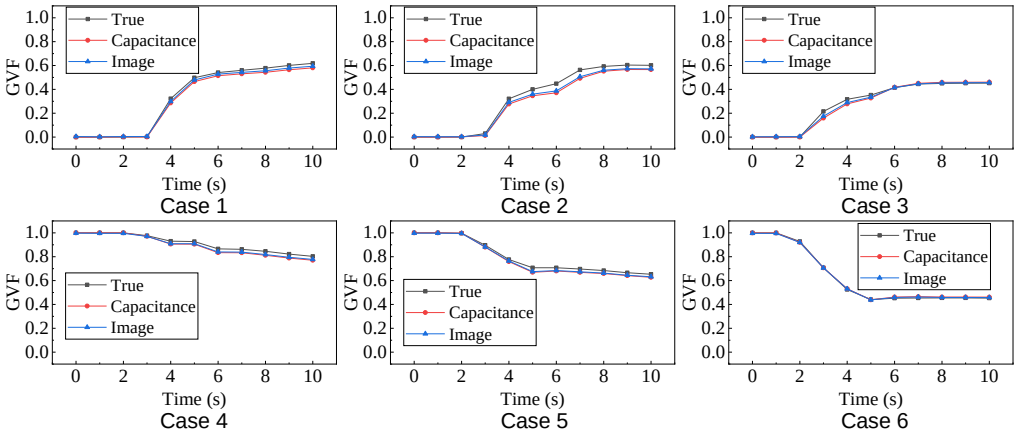

Fig. 11. GVF results using 60 dB noisy data under six simulation conditions.

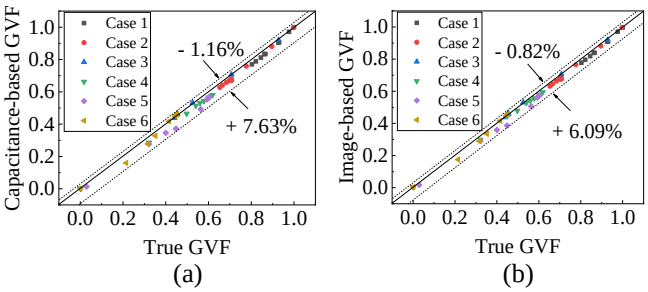

Fig. 12. Comparison of the measured GVF with the reference GVF. (a) Capacitance-based GVF. (b) Image-based GVF.

reconstructed images have visibly deteriorated, the corresponding values of the SSIM are much lower than those using noise-free or 60 dB data. Obviously, the noise with SNR of 40 dB degrades the quality and stability of the image reconstruction.

B. GVF Estimation

Two approaches, i.e. the capacitance-based and the image-based methods, are applied to calculate GVF. In this study, the capacitances with SNR of 60 dB are used to measure the capacitance-based and the image-based GVF results. The reference values for GVF are obtained by averaging the gray values of the true normalized permittivity distribution. Fig. 11 shows the GVF results under the six simulation conditions (see TABLE III). It can be seen that both the changes of the capacitance-based and image-based measurements are consistent with that of the true values. For the oil-mode simulation (cases 1-3), the initial value of GVF is 0. With the injection of the oil and gas, the GVF first increases rapidly, then increases slightly and tends to stabilize. While for the gas-mode simulation (Cases 4-6), the initial value of GVF is 1. The GVF decreases with the injection of the oil and gas, and then tends to stabilize. The full-scale errors of the capacitance-based GVF results are less than 3.82%, 7.63%, 5.60%, 3.32%, 3.84% and 1.16%, while those of the image-based GVF results are smaller than 2.44%, 6.09%, 3.97%, 2.66%, 3.29% and 0.84% for Case 1, Case 2, Case 3, Case 4, Case 5 and Case 6, respectively.

Figs. 12 (a) and (b) show the comparisons between the capacitance-based GVF and the reference GVF, and between the image-based GVF and the reference GVF, respectively. It can be found that the measurement of image-based GVF is slightly better than that of capacitance-based GVF, as the full-scale error of image-based GVF is within -0.82% to +6.09%, which is slightly smaller than that of capacitance-based GVF results (-1.16% to +7.63%), for the measurement of GVF ranging from 0 to 1. It can also be seen that, under the given conditions, both the capacitance-based and image-based GVFs are pretty close to the reference, indicating that both of the two methods are capable of achieving the accurate measurement of the GVF of the oil-gas two-phase flow. It is worth mentioning that these two GVF measurement approaches have their own advantages. For the image-based method, more accurate GVF measurement is achieved. For the capacitance-based method, the GVF can be identified directly from the inter-electrode capacitances without performing image reconstruction.

VI. CONCLUSIONS

This paper proposed a three-dimensional fluid dynamics-electrostatic field coupling model, from which the performance of ECT for the measurement of complex dynamic oil-gas two-phase flows can be quantitatively evaluated. Simulation experiments were performed to verify the feasibility of the coupling simulation of fluid field and electrostatic field. Comparative studies were also carried out to evaluate the estimated GVF and the reconstructed image quality of ECT. During the comparative experiments, two GVF measurement approaches (capacitance-based and image-based) were applied for GVF calculation, and two image reconstruction algorithms (LBP and Landweber iteration) were used for image reconstruction. Simulation experimental results indicated that the both the capacitance-based method and the image-based method using 60 dB noise data are capable of achieving the accurate GVF measurement with the full-scale error of each is within -1.16% to +7.63%, and -0.82% to +6.09% respectively, for the GVF ranging from 0 to 1, and the image reconstructed by Landweber iterative algorithm has better quality with the structural similarity is higher than 0.765. The proposed model provides a viable approach to quantify the performance of ECT and prevailing algorithms for measuring oil-gas two phase flows and can be easily extended to investigate other

multiphase flows.

Acknowledgment

The authors wish to express their gratitude to the European Union's Horizon 2020 Research and Innovation Programme under the Marie Sklodowska-Curie actions COFUND Transnational Research And Innovation Network at Edinburgh (No. 801215) and the National Natural Science Foundation of China (No. 51906209) for supporting the research.

References

[1] M. Meribout, A. Azzi, N. Ghendour, N. Kharoua, L. Khezzar, and E. AlHosani, "Multiphase flow meters targeting oil & gas industries," *Measurement*, vol. 165, p. 108111, Dec. 2020.

[2] Z. Q. Xu, F. Wu, X. M. Yang, and Y. Li, "Measurement of gas-oil two-phase flow patterns by using CNN algorithm based on dual ECT sensors with venturi tube," *Sensors*, vol. 20, no. 4, p. 1200, Feb. 2020.

[3] Z. Y. Huang, D. L. Xie, H. J. Zhang, and H. Q. Li, "Gas-oil two-phase flow measurement using an electrical capacitance tomography system and a venturi meter," *Flow Meas. Instrum.*, vol. 16, nos. 2-3, pp. 177-182, 2005.

[4] Z. Almutairi, F. M. Al-Alweet, Y. A. Alghamdi, O. A. Almisned, and O. Y. Alothman, "Investigating the characteristics of two-phase flow using electrical capacitance tomography (ECT) for three pipe orientations," *Processes*, vol. 8, no. 1, p. 51, Jan. 2020.

[5] S. N. Wang, X. L. Sun, C. L. Xu, J. T. Bao, C. Peng, and Z. Y. Tang, "Investigation of a circulating turbulent fluidized bed with a fractal gas distributor by electrostatic-immune electrical capacitance tomography," *Powder Technol.*, vol. 361, pp. 562-570, Feb. 2020.

[6] W. Q. Yang, L. H. Peng, "Image reconstruction algorithms for electrical capacitance tomography," *Meas. Sci. Technol.*, vol. 14, no. 1, pp. 1-13, Jan. 2003.

[7] K. J. Alme, S. Mylvaganarn, "Electrical capacitance tomography - Sensor model, design, simulations, and experimental verification," *IEEE Sensors J.*, vol. 6, no. 5, pp. 1256-1266, Oct. 2006.

[8] I. Ismail, J. C. Gamio, S. Bukhari, and W. Q. Yang, "Tomography for multi-phase flow measurement in the oil industry," *Flow Meas. Instrum.*, vol. 16, nos. 2-3, pp. 145-155, 2005.

[9] C. Gamio, J. Castro, F. Garcia-Nocetti, L. Aguilar, and L. Rivera, "High-pressure gas-oil two-phase flow visualization using electrical capacitance tomography," *ASME 7th Biennial Conference on Engineering Systems Design and Analysis*, no. ESDA2004-58379, pp. 475-479, Nov. 2008.

[10] Y. Li, W. Q. Yang, C. G. Xie, S. M. Huang, Z. P. Wu, D. Tsamakis, and C. Lenn, "Gas/oil/water flow measurement by electrical capacitance tomography," *Meas. Sci. Technol.*, vol. 24, no. 7, p. 074001, Jul. 2013.

[11] S. N. Wang, J. Li, M. Kong, C. L. Xu, and S. M. Wang, "Electrostatic effect on AC-Based ECT and its elimination," *IEEE Sensors J.*, vol. 17, no. 24, pp. 8081-8090, Dec. 2017.

[12] Q. Guo, S. H. Meng, D. H. Wang, Y. F. Zhao, M. Ye, W. Q. Yang, and Z. M. Liu, "Investigation of gas-solid bubbling fluidized beds using ECT with a modified Tikhonov regularization Technique," *AIChE J.*, vol. 64, no. 1, pp. 29-41, Jan. 2018.

[13] W. Q. Yang, "Design of electrical capacitance tomography sensors," *Meas. Sci. Technol.*, vol. 21, no. 4, p. 042001, Apr. 2010.

[14] Q. Marashdeh, L. S. Fan, B. Du, and W. Warsito, "Electrical capacitance tomography - A perspective," *Ind. Eng. Chem. Res.*, vol. 47, no. 10, pp. 3708-3719, May 2008.

[15] Z. Q. Cui, H. X. Wang, Z. Q. Chen, Y. B. Xu, and W. Q. Yang, "A high-performance digital system for electrical capacitance tomography," *Meas. Sci. Technol.*, vol. 22, no. 5, p. 055503, May 2011.

[16] W. Deabes, H. H. Amin, "Image reconstruction algorithm based on PSO-Tuned Fuzzy Inference System for electrical capacitance tomography," *IEEE Access*, vol. 8, pp. 191875-191887, 2020.

[17] J. M. Ye, H. G. Wang, Y. Li, and W. Q. Yang, "Coupling of fluid field and electrostatic field for electrical capacitance tomography," *IEEE Trans. Instrum. Meas.*, vol. 64, no. 12, pp. 3334-3353, Dec. 2015.

[18] J. M. Ye, H. G. Wang, and W. Q. Yang, "Evaluation of electrical capacitance tomography sensor based on the coupling of fluid field and electrostatic field," *Meas. Sci. Technol.*, vol. 27, no. 7, pp. 074003, Jul. 2016.

[19] D. L. Brown, R. Cortez, and M. L. Minion, "Accurate projection methods for the incompressible Navier-Stokes equations," *J. Comput. Phys.*, vol. 168, no. 2, pp. 464-499, Apr. 2001.

[20] E. Olsson, and G. Kreiss, "A conservative level set method for two phase flow," *J. Comput. Phys.*, vol. 210, no. 1, pp. 225-246, Nov. 2005.

[21] P. Grochowski, and J. Trylska, "Review: Continuum molecular electrostatics, salt effects, and counterion binding - a review of the Poisson-Boltzmann theory and its modifications," *Biopolymers*, vol. 89, no. 2, pp. 93-113, Feb. 2008.

[22] N. T. Liu, Y. Q. Jin, "A discussion on the effective permittivity of multi-component medium derived by Maxwell-Garnett, strong fluctuation and quasicrystalline-CP modeling," *Waves in Random and Complex Media*, DOI: 10.1080/17455030.2020.1711991.

[23] C. G. Xie, S. M. Huang, B. S. Hoyle, R. Thorn, C. Lenn, D. Snowden, and M. S. Beck, "Electrical capacitance tomography for flow imaging - system model for development of image reconstruction algorithms and design of primary sensors," *IEE Proceedings-G Circuits Devices and Systems*, vol. 139, no. 1, pp. 89-98, Feb. 1992.

[24] L. H. Peng, J. M. Ye, G. Lu, and W. Q. Yang, "Evaluation of effect of number of electrodes in ECT sensors on image quality," *IEEE Sensors J.*, vol. 12, no. 5, pp. 1554-1565, May 2012.

[25] Z. Wang, A. C. Bovik, H. R. Sheikh, and E. P. Simoncelli, "Image quality assessment: from error visibility to structural similarity," *IEEE Trans. Image Process.*, vol. 13, no. 4, pp. 600-612, Apr. 2004.